Near Real-Time Determination of Moment Tensor and Centroid Location for Northern California Earthquakes Using Broadband Waveforms from a Sparse Seismic Network.

Charles Mégnin*, Fumiko Tajima,
Douglas Dreger and Barbara Romanowicz

In preparation, May 18, 2000

*To whom correspondance should be addressed. U.C. Berkeley Seismological Laboratory, Berkeley, California 94720 (pepe@seismo.berkeley.edu)

Abstract

We present an automated system to simultaneously determine centroid earthquake location, origin time and moment tensor for regional events. This system monitors real-time seismic waveform data continuously from a sparse broadband instrument network. It inverts 5 mn moving time windows of data filtered between 20 and 50 mHz. We use between two and four stations out of a pool of six seismometers. To test the feasibility of this system we use a data set of waveforms recorded for 62 events with $M_\ell \geq 4.2$ in the northern and central California between 1993 and 1999. For those events the Berkeley Digital Seismic Network has well calibrated solutions using the established system that relies on the onset time and location information based on travel time picks from a dense short-period network. The solutions determined by the new system are compared with those available from the established system for appraisal.
Results show that onshore events with $M_w \geq 4.5$ are detected and adequately characterized by the algorithm in terms of moment tensor and centroid location on a grid of 0.5 ° intervals. The threshold value of variance reduction to detect an event is $\sim 70\%$.

In contrast, events that occured off the Mendocino coast aren't as reliably constrained, reflecting the complexity of the crustal structure that transits from oceanic to continental along the seismic ray paths inadequately represented by the present 1D model.

1 Introduction

The Berkeley Seismological Laboratory (*BSL*) has been operating a regional network (Berkeley Digital Seismic Network, *BDSN*) of 25 very broadband stations to monitor regional seismic activity in northern California (Romanowicz et al. (1992) and Romanowicz et al. (1994)). The real-time waveform data are telemetered to *BSL* over a frame-relay continuously. The broad frequency band and high dynamic range of this network is particularly suitable for efficient characterization of earthquakes (centroid location, moment-tensor (MT), and rupture dimension). In the occurrence of a large earthquake that has significant spatial dimension, it is important to know the earthquake centroid rather than the high frequency hypocenter. The current system of automated MT determination at *BSL* developed as part of the joint U.S.

Geological Survey (USGS)/*BSL* notification system, *i.e.*, Rapid Earthquake Data Integration (*REDI*) (Gee et al. (1996)), however, relies on the availability of earthquake onset-times and locations, provided to us by the USGS at Menlo Park, where they are determined in real-time from the dense array composed primarily of short-period ($\sim$ 1 sec) vertical component sensors (Northern California Seismic Network, *NCSN*).

Efforts aimed at developing a stand-alone system have recently been implemented at *BSL* with the introduction of azimuth and P and S arrival time information into the earthquake location determinations and the development of an adaptative grid search method for event location Dreger et al. (1998). This method is nevertheless largely based on the pick (*i.e.* high frequency) information of P and S waves and therefore does not take full advantage of the bandwidth of broadband waveform data. In addition, the automatic picking of S phase arrivals and the automatic determination of azimuth are not sufficiently reliable to provide a systematically accurate source location.

With the present quality of broadband seismic data, it is desirable to determine source location and MT of significant events independently of the short period data. Such a system will find a crucial application in areas of occurrence of less frequent but potentially large earthquakes where the operation of more than a few broadband stations will likely not be affordable. Kawakatsu (1998) presented basic concept and algorithms of a fully automated system that continuously monitors the background seismic wavefield and determines MT solutions for virtual point sources on a grid in the region of interest. A cost function defined on the grid is evaluated in a grid search scheme so as to identify a point source of significant variance reduction, that should corresponds to a real earthquake. The implementation of such a system will also have significant consequences for hazard mitigation as the fault mechanism and dimension are essential information to derive early estimates of strong motion near the source, as well as the location of possible aftershocks.

We tested the feasibility of a system that detects an event ($M_w \geq 4.5$) and simultaneously determines its parameters (centroid location, origin time and moment-tensor) as quickly as possible by monitoring real-time broadband waveform data from a subset of *BDSN* broadband stations that are distributed over northern and central California.

2 Theory

Following Kawakatsu (1998), we briefly describe the algorithms. A seismogram $d^k(t)$ recorded at station k can be expressed as the convolution of the response of the medium to an impulsive source $G_i^k(t)$ with the moment tensor elements m_i:

$$\Sigma_i G_i^k(t)\, m_i \;=\; d^k(t) \tag{1}$$

The solution for a moment tensor $\mathbf{m}$ is derived in the least square sense by multiplying (1) with $G_j^k(t)$ and integrating over time. The resulting normal equation is then given by:

$$\Sigma_i A_{ij}\, m_i \;=\; b_j \tag{2}$$

where

$$A_{ij} = \Sigma_k A_{ij}^k\,,\;\; A_{ij}^k \;=\; \int G_i^k(t) G_j^k(t) dt \tag{3}$$

$$b_j = \Sigma_k b_j^k\,,\;\; b_j^k \;=\; \int G_j^k(t) d^k(t) dt \tag{4}$$

Since $\underline{\mathbf{A}}$ is a square matrix, the least squares solution for the moment tensor is given by:

$$\widehat{\mathbf{m}} \;=\; \underline{\mathbf{A}}^{-\mathbf{1}}\,\mathbf{b} \tag{5}$$

where the moment tensor has been decomposed into 8 orthogonal elements corresponding to vertical strike-slip, vertical dip-slip and 45° dip-slip for the radial and longitudinal components, and strike-slip and vertical dip-slip for the transverse component (*e.g.*: Jost & Herrmann (1989)).

A measure of the variance reduction $\mathbf{VR}$ betwen data and synthetic computed for the model $\widehat{\mathbf{m}}$ can be derived by substituting (5) into (1), multiplying by the data vector and integrating over time:

$$\mathbf{VR} \;=\; \left[1 \;-\; \left(\Sigma_k \left[\int \left(d^k(t)\right)^2\, dt\right] \;-\; \mathbf{b^t}\underline{\mathbf{A}}^{-\mathbf{1}}\mathbf{b}\right)\right] \times 100 \tag{6}$$

At each grid point, a moment tensor solution which provides the best fit (maximum $\mathbf{VR}$ in equation (6)) is computed (for a perfect fit, $\mathbf{VR} = 100$). The $\mathbf{VR}$ surface described by the computation of (6) at all virtual source points over the region of interest is the critical quantity in this evaluation. The solution $\widehat{\mathbf{m}}$ which gives the maximum value of $\mathbf{VR}$ is the 'earthquake' detected that is most consistent with the long-period seismic wavefield in the time window.

3 Method and Data

Since 1993, the *BSL* determined MT solutions for 278 California events with $M_\ell \geq$3.5, out of which we selected 70 events with $M_\ell \geq$4.2 ($M_\ell \geq$4.0 in the Geyser region) for this study (see Table 1, column 1). The epicenters of these events are shown with red stars in Figure 1). In order to account for varying noise level or station distribution relative to sources across the state, the entire northern and central California is divided into 5 subregions (Figure 1):

1. Northern California, (excluding the Geysers region),
2. Geyser.
3. South of the Bay, (excluding the Mammoth region),
4. Mammoth,
5. Offshore Mendocino,

We pay special attention to events that originate in the Mammoth and the Geyser regions as the presence of source complexity with possible non-double couple components may need to be accounted for in the source mechanisms (*e.g.* Dreger et al. (2000)).

We use 5 minute time windows of data recorded at up to 6 *BDSN* broadband stations: BKS, CMB, HOPS, ORV, SAO, and YBH (See Table 2 and the green triangles in Figure 1). The length of the time window is chosen to include all body and surface waves at any station for any event within the region. The source parameters are determined using the hybrid grid search and direct inversion scheme as described above. The double couple (DC) and compensated linear vector dipole (CLVD) components of the moment tensor are determined by solving the equation (5), and the other parameters (centroid location and origin time) are obtained from the grid search scheme.

Before inversion, we calculated Green's functions in (1) using the frequency-wavenumber integration method of Saikia (1994) for two layered models: Socal (Dreger & Helmberger (1993)) and *GIL7* (Dreger & Romanowicz (1994)) (see Table 3 and Figure 2), and tabulated them.

Empirically, earthquakes located in the western part of the state are modeled well using *GIL7* which has a slower upper crust, and those in eastern California with *SoCal*. Figure 3 shows the relation between virtual point source location and the models used: *GIL7* with open circles, and *SoCal* with filled circles. For each model, we construct a catalog of Green's functions corresponding to distances between 45 and 900 km with an increment of 5 km and for source depths between 5 and 39 km, with an increment of 3 km, for a total of $2\,(\text{models}) \times 172\,(\text{distances}) \times 12\,(\text{depths}) = 4,128$ sets of 8 orthogonal elementary moment tensors.

For each earthquake, we invert for moment tensor and origin time at 160 virtual locations distributed over the grid with a half-degree interval. Once a solution is obtained on the initial grid, we seek a more accurate location by 'zooming' in on the area described by an 80 km circle around the initial source location, over which we overlay a new grid with a $0.25°$ interval for about 31 virtual source locations.

4 Test Inversions

An important issue in evaluating the feasibility is whether a unique solution can be identified both in space and time during the occurrence of a real seismic event. Thus we investigate the conditions under which an optimal solution of the centroid location and moment-tensor can be unequivocally determined from a maximum **VR**. We address this issue by performing inversions for point source location and origin time seperately (see the summary in Table 4) using events with $M_\ell \geq 4.2$ that occurred in Northern California and recorded by *BDSN*.

4.1 Preliminary considerations

The original data set consisting of 70 events was initially screened by rejecting data that showed poor signal to noise ratio (*SN*). The 62 events remaining after this step were inverted (see Table 1, column 2) and constitute the basis of our analysis.

We estimated an optimal frequency band by inverting the data set in the 20-50 mHz and 10-100 mHz bands. The fit to the data proved far superior in the 20-50 mHz band range, suggesting that 3D effects should be incorporated in the calculations in order to benefit from broader band information.

The data are inverted for MT and source depth at each of all the virtual source locations. A value for **VR** (equation (6)) is computed at all the grid points, thereby describing a **VR** surface over the region. An optimal solution or automated moment tensor solution (*AMT* hereafter) is determined for the source parameters (i.e., centroid location and MT) at the point where the maximum **VR** is found.

Seismic stations

Although up to six stations can be used, long range propagations sometimes cause systematic errors due to unmodeled path effects. Preliminary inversions resulted in some cases with events displaying high mislocation and poor **VR**, although the *SN* ratio was high. The waveforms for such events displayed noticeable energy in the coda at some stations which corresponded to long Central Valley travel paths. For such source-receiver distribution, the 1D Green's functions failed to reproduce these signals in waveforms. The San Felipe event of 8/11/1993, $M_\ell = 4.6$, is an example of such contamination (Figure 4). The source location (red star), the source-receiver paths (blue lines), and the stations (green triangles) are shown. The bottom left figure represents the raw data and the bottom right figure the data filtered between 20 and 50 mHz. The coda signal is prominent at stations ORV and YBH for which the source-receiver distribution results in long travel paths through the Central Valley.

For each virtual source location, we therefore only use stations which avoid long Central Valley travel time. In Table 5, we show the seismic stations used for source location in different subregions.

4.2 Spatial Inversion

In this section, we show examples of inversions for source mechanism and centroid location in each of the five regions.

Figure 5 (top) shows an example of spatial inversion for a 1999/08/18, $M_\ell = 5.0$ Bolinas event recorded, at the point of maximum **VR**, at stations CMB & SAO (shown with the green triangles). Each small circle showing a grid point is color-coded according to the variance reduction. The red source mechanism shows the *AMT* solution at $122.5°W$ and $38.0°N$, and an $M_w = 4.6$ (with **VR**=89.7%). The red star represents the "ground truth" locations determined by the *REDI* system for the reference. The blue 'beach ball' corresponds to the *REDI* moment tensor. A unique solution in good agreement with the benchmark is obtained.

In Figure 6, we investigate the spatial stability of the solution by showing the variation of the mechanisms about the solution of Figure 5 (top), on the fine $0.25° \times 0.25°$ grid. The small numbers above the beach balls represent the **VR**s for the virtual point sources. The top figures suggest strong dependence of source mechanism and **VR** on the epicentral location, but the objective function displays a well-isolated peak with little variation in mechanism about the maximum **VR**. The bottom figures show the mechanisms computed for source depths between 5 and 39 km with the epicenter location fixed at the maximum **VR** point. In this example, the mechanisms remains relatively stable for different source depths, in agreement with the results of Kawakatsu (1998).

Figure 7 (top) shows the spatial objective function for a 1995/09/04, $M_\ell = 4.5$ Geyser event, recorded at stations ORV & SAO. The M_w derived was 4.9 and a **VR** of 85.8% was obtained. Figure 8 shows the mechanism variation about the solution on the fine grid, displaying a stable solution both horizontally and vertically.

Figure 9 (top) shows the spatial objective function for a 1998/08/12, $M_\ell = 5.4$ San Juan Bautista event, recorded at stations BKS & CMB. The M_w derived was 5.1 and a **VR** of 93.8% was obtained. The variation in mechanism shown in Figure 10 also displays a stable solution in the horizontal and vertical planes.

Figure 11 (top) shows the spatial objective function for a 1997/12/31, $M_\ell = 4.8$ Mammoth event, recorded at stations ORV, CMB & SAO. The M_w derived was 4.8 and a **VR** of 92.4% was obtained. The mechanism variation of Figure 12 is stable.

Figure 13 (top) shows the spatial objective function for a 1995/02/19, $M_\ell = 6.8$ Mammoth event, recorded at stations ORV, CMB & YBH. The M_w derived was 6.6 and a **VR** of 90.4% was obtained. The mechanism variation shown in Figure 14 is also stable.

Although useful, the spatial inversion does not allow to examine multiple local minima that may exist as a function of time. We now explore this issue:

4.3 Origin Time Inversion

The presence of local minima in real-time data inversion would result in error in the determination of the origin time, which in turn could affect all other source parameters. To assess the stability of the solution in time, we inverted the same data sets as above for a source at the fixed epicenter determined by *REDI* (see Table 4, second row). We performed successive inversions for an optimal MT, allowing the origin time to vary over a period of 2 min around the *REDI*-determined solution in increments of 1 second. This time window was sufficient to isolate a unique mininum. Examples of such inversions are shown at the bottom of Figures 5, 7, 9, 11 and 13 for the events discussed in the previous section. The *REDI* origin time is shown with a red vertical line, and the solid curve represents the variance reduction as a function of origin time. In all these examples, we note the presence of local minima in the variance reduction. This is caused by the cross correlation of the surface waves, coming in and out of phase with each half-period in the moving time window. Nevertheless, in all cases studied, the variance reduction corresponding to the local minima proved significantly lower than that of the global minimum. We therefore do not expect that the presence of local minima would impact the results of forthcoming inversions. Except for the Mendocino event, good agreement is found between the AMT and the *REDI* origin time. We discuss the particular case of offshore Mendocino earthquakes below.

4.4 Summary of results

Figure 15 show the quality of the AMT locations as a function of M_w cut-off for all events (top Figure), onshore events (middle Figure) and Offshore Mendocino events (bottom Figure). We have divided the solutions in three quality batches, defined by the horizontal distance between AMT and *REDI* solutions: the Q1 batch corresponds to mislocations of less than 40 km, Q2 mislocations greater than 40 km but less than 80 km, and the Q3 batch the others. The top Figure shows an overall significant proportion of poor quality solutions (belonging to batch Q3). However, this is due exclusively to the Mendocino data set as the onshore events all correspond to good (Q1) or acceptable (Q2) solutions, from an M_w cutoff of 4.2. We attribute the quality of the Mendocino data to the complexity of the offshore crustal structure, poorly represented with our present 1D velocity model.

As we are primarily concerned with issues of hazard mitigation we have restricted our analysis to the 32 events with a moment magnitude greater than 4.5 (see Table 1, column 3). This provides us with a margin of security above the 4.2 cutoff determined above. We have also eliminated from the analysis solutions derived with a single station as these proved unreliable.

In Table 6 (center column), we show the details of the solutions on the half-degree grid for the 23 onshore event with $M_w \geq 4.5$. Table 7 shows the solutions for the 9 Mendocino earthquakes. The subcolumns represent the M_w derived, the variace reduction, the horizontal mislocation parameter Δ representing the lateral distance between *AMT* and *REDI* solutions, the vertical mislocation parameter δz representing the difference in depth between *AMT* and *REDI* solutions, and μ is the scalar difference between moment tensors $M_{ij}^{(1)}$ and $M_{ij}^{(2)}$ defined by Pasyanos et al. (1996) and given by:

$$\mu \equiv \sqrt{\frac{\sum_{i=1}^{3} \sum_{j=1}^{3} \left(\delta M_{ij}^{'} \right)^2}{8}} \tag{7}$$

where $\delta M_{ij}^{'} \equiv M_{ij}^{(1)'} - M_{ij}^{(2)'}$ and $M_{ij}^{'} \equiv \frac{M_{ij}}{M_0}$, and M_0 is the seismic scalar moment. Focal mechanisms are essentially equivalent for $\mu < 0.25$ and are significantly different for $\mu > 0.50$ (Pasyanos et al. (1996)).

Examination of Table 6 indicates that the minimum **VR** level that detects an event of $M_w \geq 4.5$ is about 70%. A similar threshold is obtained for offshore events (Table 7), but given the high number of medium to low quality solutions, we consider the present system inadequate for the proper characterization of such earthquakes.

4.5 Inversion of a moving time-window

To simulate the system response to the continuous inversion of incoming seismic waveforms, we invert successive windows of 5 minutes of data about the origin time of the 12/20/1994 Parkfield, CA event (M_ℓ=4.7, origin time 10:27:48), separated by 20 second intervals. This experiment is displayed as an animation in the attached mpeg file, and the major time steps are also shown in Figures 16 through 19.

Method

We perform continuous inversions of moving windows of the seismic wavefield for moment tensor and centroid depth, on the 0.5° by 0.5° degree grid (the circles) overlaying northern and central California. The value of **VR** in each window is indicated in front of 'VR' in the top right legend and is color-coded on the maps.

In this simulation, the time windows are five minutes long and each successive window is shifted by 20 seconds with respect to the previous one, simulating data recorded by the seismic stations in real-time. The starting time of each moving window is given by the value t_0 in the legend at the top of each frame. The data is shown for the 4 broadband *BDSN* stations used (green triangles on the map at BKS, CMB, ORV, and SAO) at the bottom of the plot. Recordings at staions HOPS and YBS had a poor *SN* ratio and were discarded. Each trace is scaled to its maximum amplitude. The traces on the left are the raw data and those on the right are in the frequency band between 20 and 50 mHz (that used in the inversion). Only the vertical component of each seismic trace is shown here, but we invert 3 component data.

We show for comparison the *REDI* MT solution with the (fixed) blue beach ball and the *REDI* epicenter location with the red star, as in Figures 5, 7, 9, 11 and 13. The best solution corresponding to each time window is represented by the red beach ball, which points to the optimal epicentral location. The best automated moment tensor solution for this event yielded a variance reduction of 93% (color-coded orange), achieved in the five successive five-minute time windows beginning between 09:52:20 and 09:53:40.

Results

In the first few frames, not enough data is present in the inverted time window to yield an optimal solution: the value of **VR** is low everywhere, and the successive solutions display spatial variability with time. Figure 16 shows the fourth frame spanning the time window between 10:24:00 & 10:29:00. The **VR** is 31.9%, well below detection threshold.

Starting with the 11th frame (Figure 17), the seismic wavefield generated by the event is present in the window and convergence to the *REDI* location/moment tensor is observed. The **VR** reaches 90.5% and the *AMT* algorithm 'zooms in' on the area 80 km around the best solution, computing a new set of moment tensor solutions on the 0.25° degree grid, improving the centroid location by 9.2 km (frames 12 13 14, Figure 18). Frames 15 to 18 yield the same solution as frame 11 since they contain the entirety of the wavefield generated by the earthquake.

Figure 19 corresponds to frame 22, and shows the objective function after the front part of the seismic wavetrain has left the window. *AMT* and *REDI* solutions start diverging.

5 Discussion

We have shown that it is possible to monitor the seismic activity in northern California with seismic waveforms consinuously recorded by a sparse network of broadband stations without relying on onset time information. The system we developed allows the determination of an accurate location and moment tensor for events at least with an $M_w \geq 4.5$. We have shown that it provides a unique solution in space and time for all event studied. The threshold variance reduction indicative of the occurence of an event is about 70% for onshore events. For offshore Mendocino earthquakes, the 1D model *GIL7* we use is inadequate to provide source location and MT with the same accuracy.

This methodology is particularly relevant to the seismic monitoring of regions of the world exposed to significant seismic risk, but where the implementation of a dense seismic network will not take place. It will also offer a starting point to incorporate finite source effects (Kaverina et al. (1998)) and rapidly produce a map of ground shaking caused by an earthquake.

CPU

A critical issue in this system is the time needed to detect an event and obtain its MT solution. Figure 20 shows the CPU time necessary to compute MT solution for a point source on a 248 MHz Ultra-Sparc 2 workstation. Roughly speaking, the CPU time is proportional to the number of stations used in the inversion, and on average about 1.5 sec for one station (Figure 20, blue line). The CPU time necessary to compute the cost function in series over the entire region using typically 3 or 4 stations is therefore:
$4\,(\text{stations}) \times 1.5\,(\text{seconds}) \times 160\,(\text{grid points}) = 16\,\text{min}.$

However, in this benchmark, the set of Green's functions are read from the disk at each virtual source point, a process which significantly affects computation time. The amount of cpu spent during this I/O step is 0.4s, for an average of 1.1 second for each station used (Figure 20, red line). In the parallel version of the code, the Green's functions will be stored in memory once and for all. We therefore estimate that the time necessary to invert the seismic wavefield is:

$$4\,(\text{stations}) \times 1.1\,(\text{seconds}) \times 160\,(\text{grid points}) = 11\,\text{min}\,45\,\text{seconds}.$$

False Alarms

To determine whether event detection could be falsely triggered, we performed inversions of five minute time windows windows of a seismically quiescent time series. The highest variance reduction associated with this inversion never exceeded 30%, thereby indicating that background noise alone is unlikely to be interpreted as an earthquake.

Another possible source of false triggering is the mapping of teleseisms as regional events. Although the absence of such a phenomenon in the future cannot be assessed, we performed a test with several teleseismic events of magnitude greater than 7.0. The inversion of data from such earthquakes also didn't exceed 30%, indicating that the mapping of teleseisms as regional events in northern California is unlikely to occur.

Zooming

The results of Table 6 allow to investigate the benefit associated with the zooming step in terms of the improvement in solution it provides. This is summarized Table 8 for each region and for each of the three comparison parameters: horizontal distance, vertical distance, and scalar moment tensor difference. On average, the zooming does not provide an improved solution. This indicates that the limit of the resolution attainable with 20 mHz waveforms in somewhere between 0.5° and 0.25°.

Acknowledgements: We thank H. Kawakatsu for providing us with preprints of his study before its publication and for fruitful discussions. All figures were prepared using GMT (version 3.3) Wessel & Smith (1991).

References

Dreger, D. S. & Helmberger, D. V., 1993, Determination of source parameters at regional distances with three-component sparse network data, *J. Geophys. Res.*, **98**, 8,107–8,125.

Dreger, D. S. & Romanowicz, B., 1994, Source characteristics of events in the san francisco bay region, *U.S. Geol. Surv.*, **Open-File Rept. 94-176**, 301–309.

Dreger, D. S., Uhrhammer, R. A., Frank, J., & Romanowicz, B., 1998, Regional and far-regional earthquake locations and source parameters using sparse broadband networks: A test on the ridgecrest sequence, *Bull. Seism. Soc. Am.*, **88**, 1,353–1,362.

Dreger, D. S., Tkalčić, H., & Johnston, M., 2000, Dilatational processes accompanying earthquakes in the long valley caldera, *Science*, **288**, 122–126.

Gee, L., Dreger, D. S., Neuhauser, D., & Romanowicz, B., 1996, The redi program, *Bull. Seism. Soc. Am.*, **86**, 936–945.

Jost, M. L. & Herrmann, R. B., 1989, A student's guide to and review of moment tensors, *Seism. Res. Lett.*, **60, No 2**, 37–57.

Kaverina, A., Dreger, D. S., & Antolik, M., 1998, Source process of the 21 april 1997 santa cruz island earthquake (m_w 7.8), *Geophys. Res. Lett.*, **25, No 21**, 4,027–4,030.

Kawakatsu, H., 1998, On the realtime monitoring of the long-period seismic wavefield, *Bull. Earthq. Res. Inst.*, **73**, 267–274.

Pasyanos, M. E., Dreger, D. S., & Romanowicz, B., 1996, Toward real-time estimation of regional moment tensors, *Bull. Seism. Soc. Am.*, **86 No 5**, 1,255–1,269.

Romanowicz, B., Gee, L., & Uhrhammer, R. A., 1992, Berkeley digital seismic network: a broadband network for northern and central california, *IRIS Newslett.*, *XI*, 1–5.

Romanowicz, B., Neuhauser, D., Bogaert, B., & Oppenheimer, D., 1994, Accessing northern california earthquake data via the internet, *EOS Trans. AGU*, **75**, 258–261.

Saikia, C. K., 1994, Modified frequency-wavenumber algorithm for regional seismograms using filon's quadrature, modelling of lg waves in eastern north america, *Geophys. J. Int.*, **118**, 142–158.

Wessel, P. & Smith, W. H. F., 1991, New version of the Generic Mapping Tool released, *EOS Trans. AGU*, **72 441**, 445–446.

Source region	Initial events ($M_l \geq 4.2$)	'Clean' events	Events used ($M_w \geq 4.5$)
Northern California	9	9	5
Geysers	3	3	1
South of the Bay	14	11	6
Mammoth	25	25	11
Mendocino (offshore)	19	14	9
Total	70	62	32

Table 1 Number of events used in the study. Column 1: Initial pool of events with $M_l \geq 4.2$. Column 2: Number of events after removal of noisy data. Column 3: Number of remaining events with $M_w \geq 4.5$ computed with at least two stations.

Station	Latitude	Longitude
BKS	37.877	-122.235
CMB	38.035	-120.385
HOPS	38.9935	-123.0723
ORV	39.556	-121.500
SAO	36.765	-121.445
YBH	41.7318	-122.7105

Table 2 Stations used in the study.

GIL7				SoCal			
V_p km/s	V_s km/s	ρ g/cc	Z km	V_p km/s	V_s km/s	ρ g/cc	Z km
3.20	1.50	2.28	0.0	5.50	3.18	2.40	0.0
4.50	2.40	2.28	1.0	6.30	3.64	2.67	5.5
4.80	2.78	2.58	3.0	6.70	3.87	2.80	16.0
5.51	3.18	2.58	4.0	7.80	4.50	3.30	35.0
6.21	3.40	2.68	5.0				
6.89	3.98	3.00	17.0				
7.83	4.52	3.26	25.0				

Table 3 The two models of California crust and uppermost mantle used in the computation of the Greens functions (see figure 2).

Inversion Type	Epicenter	Depth	MT	OT
Spatial	GS	GS	DI	XC
Temporal	Fixed (REDI)	GS	DI	GS

Table 4 Summary of inversions. MT=moment tensor, OT=origin time, DI=direct inversion from (5), XC=Cross-correlation, GS=Grid search.

Virtual source location	Coordinates		Stations used
	Latitude	Longitude	
No Cal	$\geq 38.5°$	$-124.5°$ to $-122°$	BKS CMB ORV YBH
Geysers	$39.1°$ to $38.5°$	$-123°$ to $-122.5°$	BKS HOPS ORV
South of the Bay (West)	$< 38.5°$	$< -120°$	BKS CMB SAO
South of the Bay (East)	$< 38.5°$	$\geq -120°$	CMB ORV SAO
Mendocino (offshore)	$\geq 39.5°$	$\leq -124.5°$	CMB HOPS ORV YBH

Table 5 Stations used for each virtual source region.

				0.5° grid					0.25° grid				
Date	Time	Location	# stns	M_w	VR (%)	Δ (km)	δz (km)	μ	M_w	VR (%)	Δ (km)	δz (km)	μ
Northern California													
11/15/1995	20:33	Truckee	3	4.5	79.3	63.5	8.0	0.42	4.5	71.3	14.6	8.0	0.22
07/21/1998	08:38	Redding	3	4.5	87.5	19.1	10.0	0.25	4.5	73.8	16.1	1.0	0.18
10/30/1998	09:53	Truckee	4	4.8	93.4	5.5	13.4	0.14	4.8	92.4	23.7	13.4	0.06
11/26/1998	22:58	Redding	3	5.2	69.6	15.0	-3.6	0.46	5.2	86.3	18.2	8.4	0.45
08/18/1999	01:06	Bolinas	2	4.5	89.7	19.4	1.3	0.15	4.5	89.7	19.4	1.3	0.15
Geysers													
09/04/1995	14:16	Healdsburg	2	4.8	85.8	41.7	16.3	0.38	4.8	94.3	7.4	10.3	0.31
South of the Bay													
08/11/1993	22:33	S.Felipe	3	4.7	93.2	9.3	1.6	0.14	4.7	92.7	38.1	4.7	0.05
11/14/1993	12:25	Parkfield	3	4.8	92.9	22.5	-3.7	0.12	4.8	92.3	5.3	-0.7	0.14
12/20/1994	10:27	Parkfield	3	5.0	92.1	18.9	-4.1	0.21	5.0	90.5	9.7	-4.1	0.15
04/23/1995	08:41	Pinnacles	2	4.9	95.4	16.9	3.2	0.16	4.9	93.9	29.0	0.2	0.12
05/21/1996	20:50	S.Jose	2	4.8	75.3	44.5	18.9	0.55	4.8	75.3	44.5	18.9	0.55
08/12/1998	14:10	S.JuanBta	2	5.1	94.8	3.3	1.7	0.18	5.1	93.8	27.6	4.7	0.18
Mammoth													
11/02/1997	08:51	Crossing,NV	3	5.2	90.8	45.0	-5.0	0.20	5.2	91.6	19.7	-8.0	0.14
11/22/1997	12:06	Mammoth	3	4.5	77.1	16.7	15.6	0.52	4.5	78.3	19.5	-3.4	0.12
11/22/1997	17:20	Mammoth	3	4.9	85.8	16.2	3.3	0.29	4.9	86.7	43.3	6.3	0.32
11/22/1997	18:10	Mammoth	3	4.5	90.2	15.5	5.8	0.16	4.5	92.4	23.1	8.8	0.14
11/30/1997	21:17	Mammoth	3	4.9	86.7	15.6	3.9	0.23	4.9	87.8	42.9	3.9	0.31
12/31/1997	20:36	Mammoth	3	4.8	92.4	35.8	-1.6	0.23	4.8	92.4	35.8	-1.6	0.23
03/20/1998	10:43	Nevada	2	4.8	93.0	55.7	-2.2	0.29	4.8	94.5	20.4	-2.2	0.29
06/09/1998	05:24	Mammoth	3	4.9	92.1	70.4	1.2	0.31	4.9	93.8	37.8	4.2	0.25
07/15/1998	04:53	Mammoth	3	5.0	94.3	28.0	-1.2	0.11	5.0	94.8	35.2	-1.2	0.39
05/15/1999	13:22	Mammoth	3	5.5	85.4	28.2	-0.6	0.13	5.5	87.0	41.9	-0.6	0.14
05/15/1999	17:54	Mammoth	3	4.6	78.1	29.3	0.7	0.97	4.6	79.0	27.7	0.7	4.52

Table 6 Summary of results for onshore events ($M_w \geq 4.5$) for 0.5° and 0.25° grid spacing. Δ is the mislocation defined as the lateral distance (in kilometers) between the *REDI* and the *AMT* solutions. δz is the difference in depth (in kilometers) between the solutions. μ is the scalar difference between *REDI* and *AMT* solutions defined in (7).

				0.5° grid					0.25° grid				
Date	Time	Location	# stns	M_w	VR (%)	Δ (km)	δz (km)	μ	M_w	VR (%)	Δ (km)	δz (km)	μ
Mendocino													
10/23/1993	18:45	Petrolia	3	4.8	80.1	64.3	27.9	0.32	5.1	81.3	70.3	33.9	0.32
06/19/1994	10:39	Petrolia	3	4.9	87.4	48.2	7.8	0.09	4.9	87.7	75.7	7.8	0.26
09/01/1994	15:15	Mendocino	3	6.9	76.2	60.6	18.3	0.09	6.9	77.5	81.7	18.3	0.09
12/26/1994	14:10	Eureka	4	5.4	77.2	33.4	-2.5	0.07	5.4	82.8	29.4	0.5	0.10
02/19/1995	04:03	GordaPlate	3	6.6	90.4	53.5	18.7	0.17	6.6	91.0	19.1	18.7	0.11
03/01/1995	10:55	OffshorePet.	3	4.6	83.6	32.1	0.0	0.20	4.6	84.4	50.3	0.0	0.11
08/08/1996	09:19	Petrolia	4	4.7	85.9	65.6	21.0	0.14	4.7	87.0	64.6	18.0	0.11
01/22/1997	07:17	Mendocino	2	5.6	62.3	184.9	3.4	0.70	5.6	69.7	220.1	15.4	0.63
11/27/1998	00:43	OffshorePet.	4	5.4	84.7	46.0	12.7	0.30	5.4	84.7	46.0	12.7	0.30

Table 7 Same as Table 6 for offshore Mendocino events ($M_w \geq 4.5$) for 0.5° and 0.25° grid spacing.

	Δ			δz			μ		
Event location	Imp./ Unaf.	Det. (#)	Mean (km)	Imp./ Unaf.	Det. (#)	Mean (km)	Imp./ Unaf.	Det. (#)	Mean
Northern California	3	2	6.1	4	1	-0.6	5	0	.07
Geysers	1	0	34.3	1	0	6	1	0	.07
South of the Bay	3	3	-6.5	4	2	-1.	5	1	.03
Mammoth	5	6	0.8	7	4	1.2	6	5	-0.3
Total onshore	12	11	1.5	16	7	0.4	17	6	-0.12
Mendocino	4	5	-7.6	7	2	-2	7	2	0.0
Total	16	16	-1.0	23	9	-0.3	24	8	-0.1

Table 8 Improvement of the solution as a result of 'zooming'. Imp. = Improved; Unaf = unaffected; Det. = Deteriorated. First column: in term of the horizontal distance Δ. Second column: in term of the vertical distance δz. Thirm column: in term of the MT scalar difference parameter μ. Improvement in the mean value for each parameter is given by a positive number.

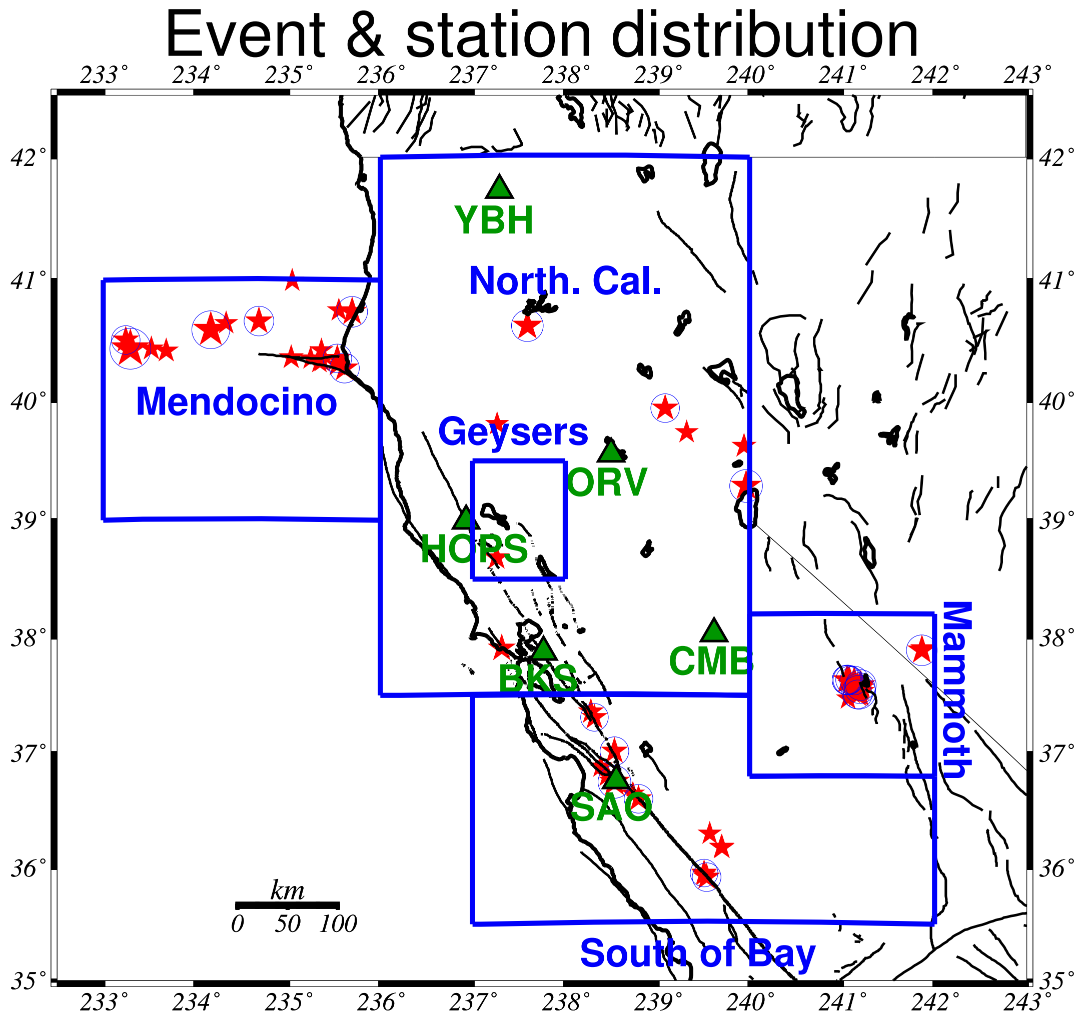

Figure 1 REDI-determined location of the 62 events used in this study. The blue circles represent the 32 events with $M_w \geq 4.5$.

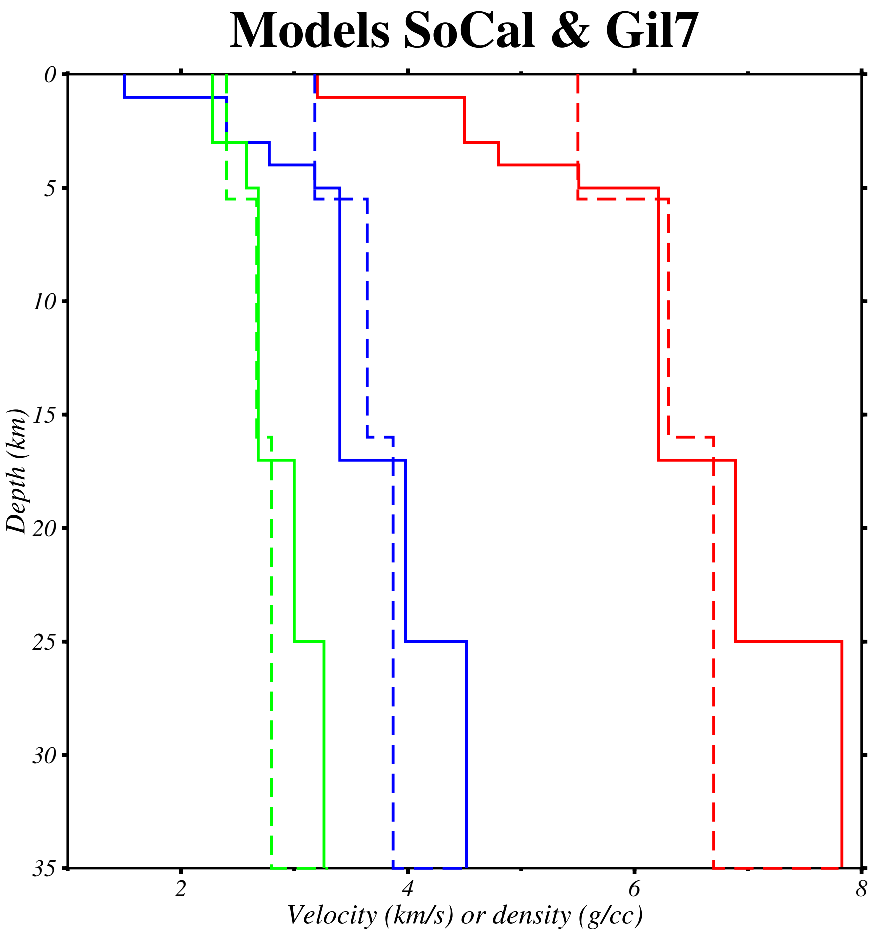

Figure 2 Models used in this study. Solid line: GIL7, dashed line: SoCal. Red: V_p, Blue: V_s, Green: ρ.

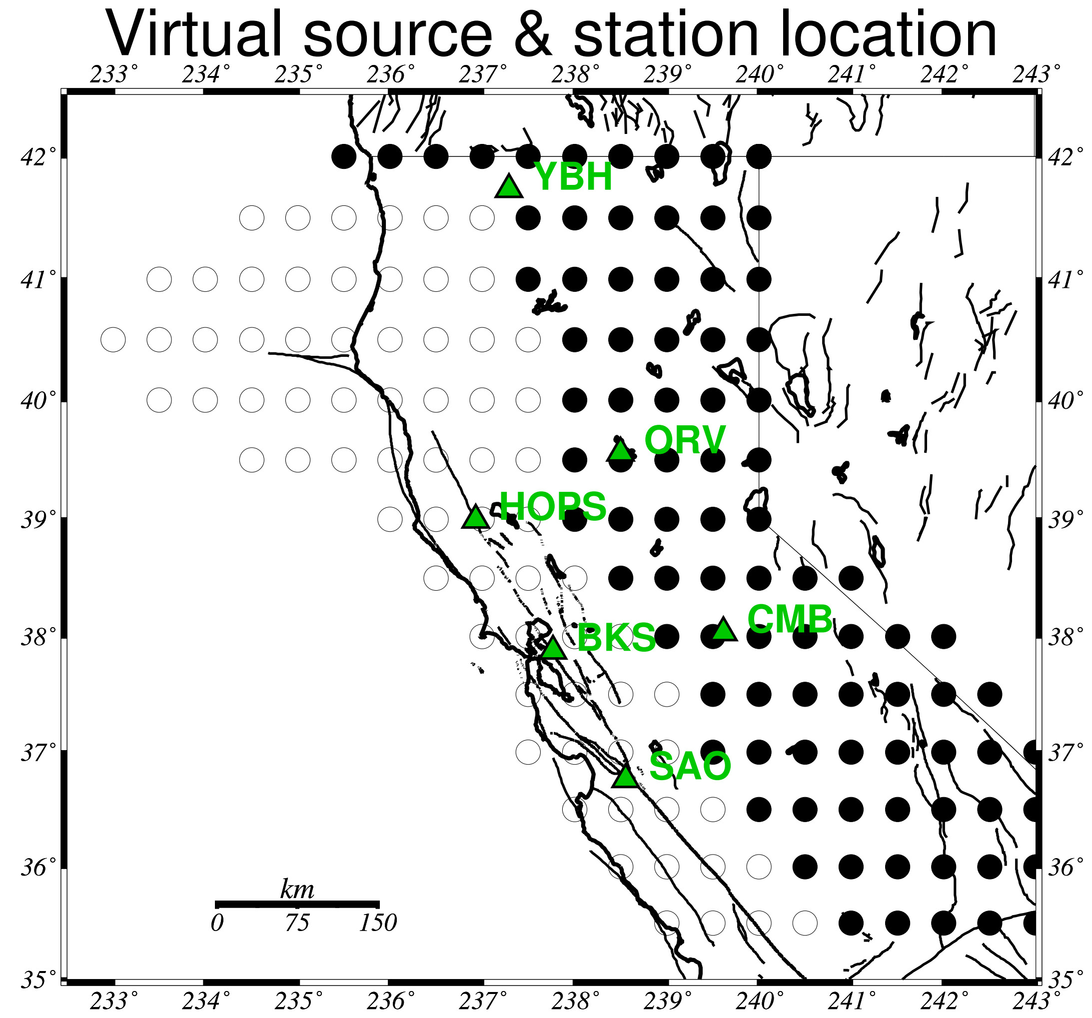

Figure 3 Virtual source grid (160 circles) and station (6 triangles) locations. The circles correspond to the model used as a function of the source location. Empty circles: GIL7. Filled circles: SoCal.

Ray paths San Felipe (08/11/1993)

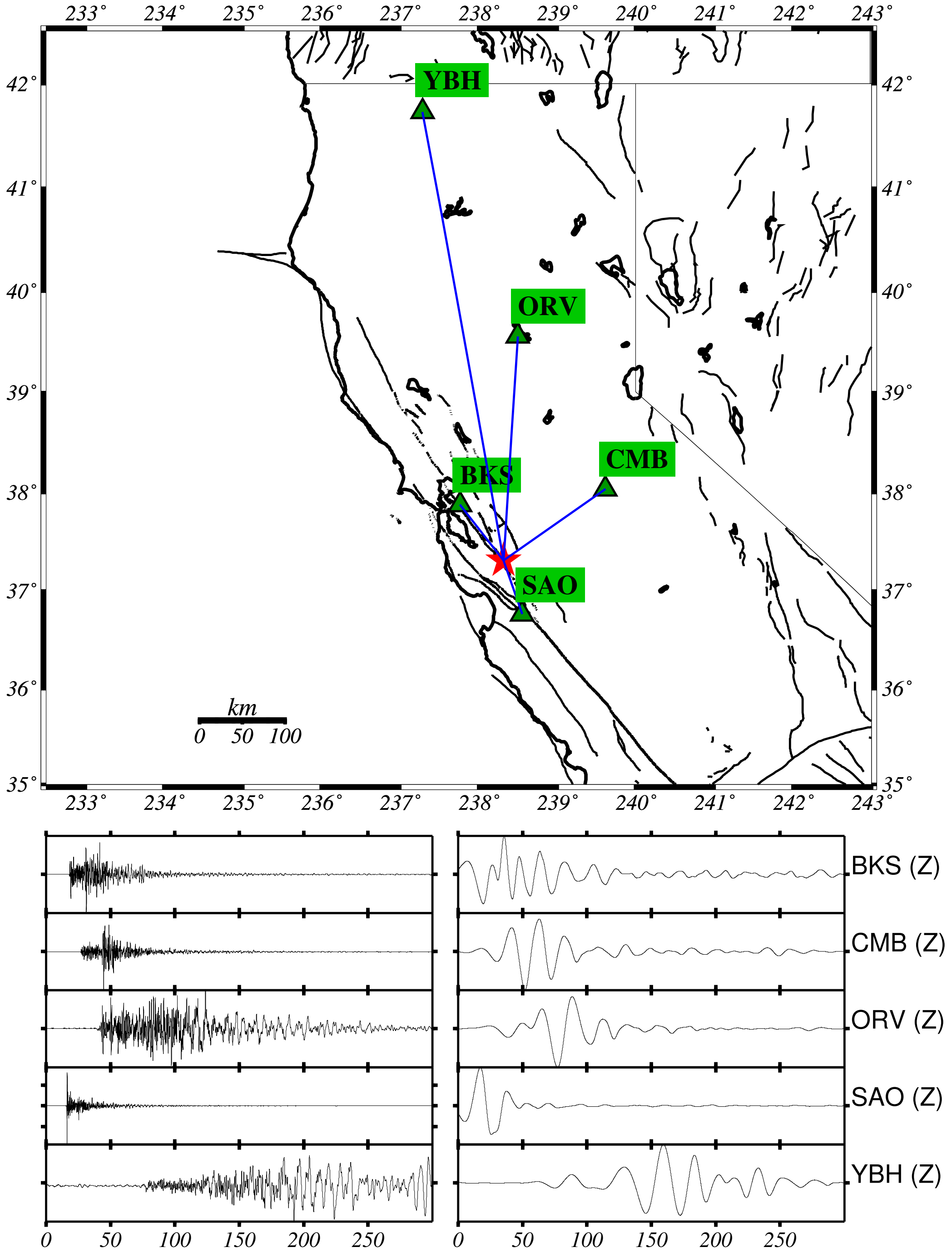

Figure 4 Waveforms for the 8/11/1993 San Felipe event ($M_\ell = 4.6$). Top: Source-receiver paths. Bottom: data - Raw (left) and filtered in the 20-50 mHz band (right).

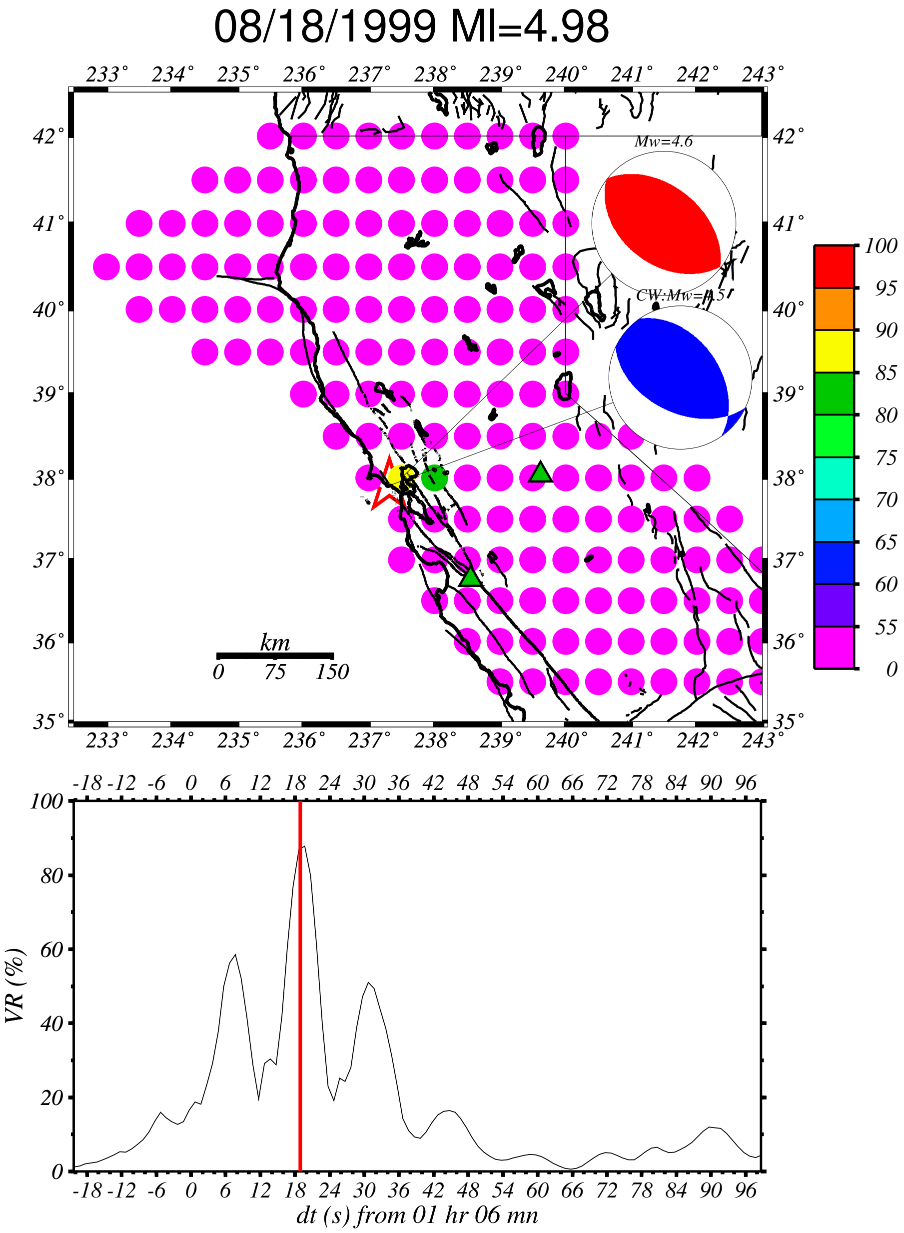

Figure 5 Example of spatial (top) and temporal (bottom) objective functions for the 1998/08/18, $M\ell = 5.0$ Bolinas event. Top: The red star represents the epicenter of the *REDI*-derived solution. The yellow triangles are the stations used for this particular earthquake. The red 'beach-ball' points to the location of the best solution with variance reduction of 89.7%. The blue 'beach ball' is the reference *REDI* moment tensor. Bottom: Variance reduction as a function of origin time at the *REDI* location. The vertical dashed line is the *REDI*-derived origin time.

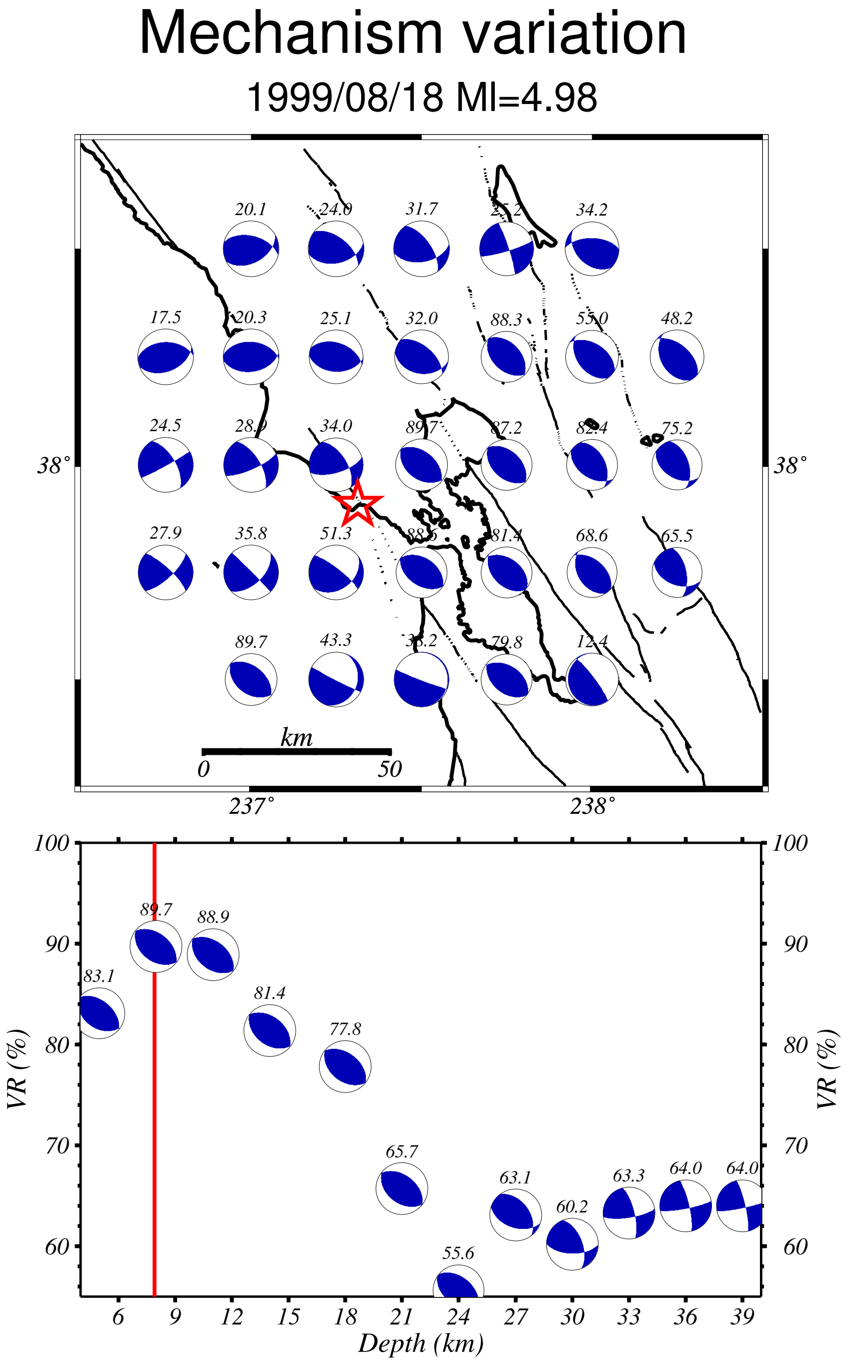

Figure 6 Variation of the source mechanisms for the Bolinas event of figure 5 as a function of: (Top) source location near the solution (122.5°W and 38.0°N); (bottom): source depth. The variance reduction for each moment tensor is indicated above the beach balls.

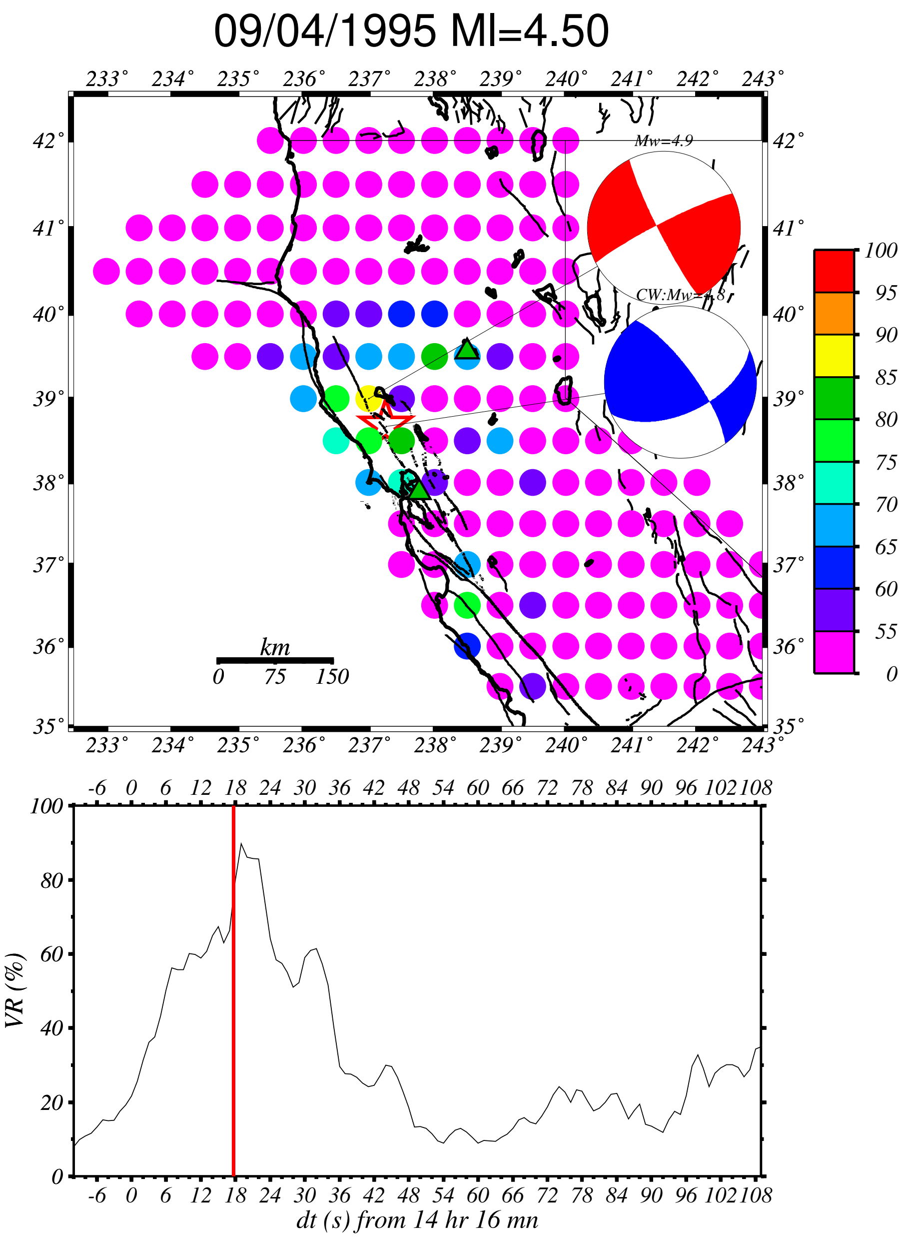

Figure 7 Same as Figure 5 for a 1995/09/04, $M\ell = 4.5$, Geyser event.

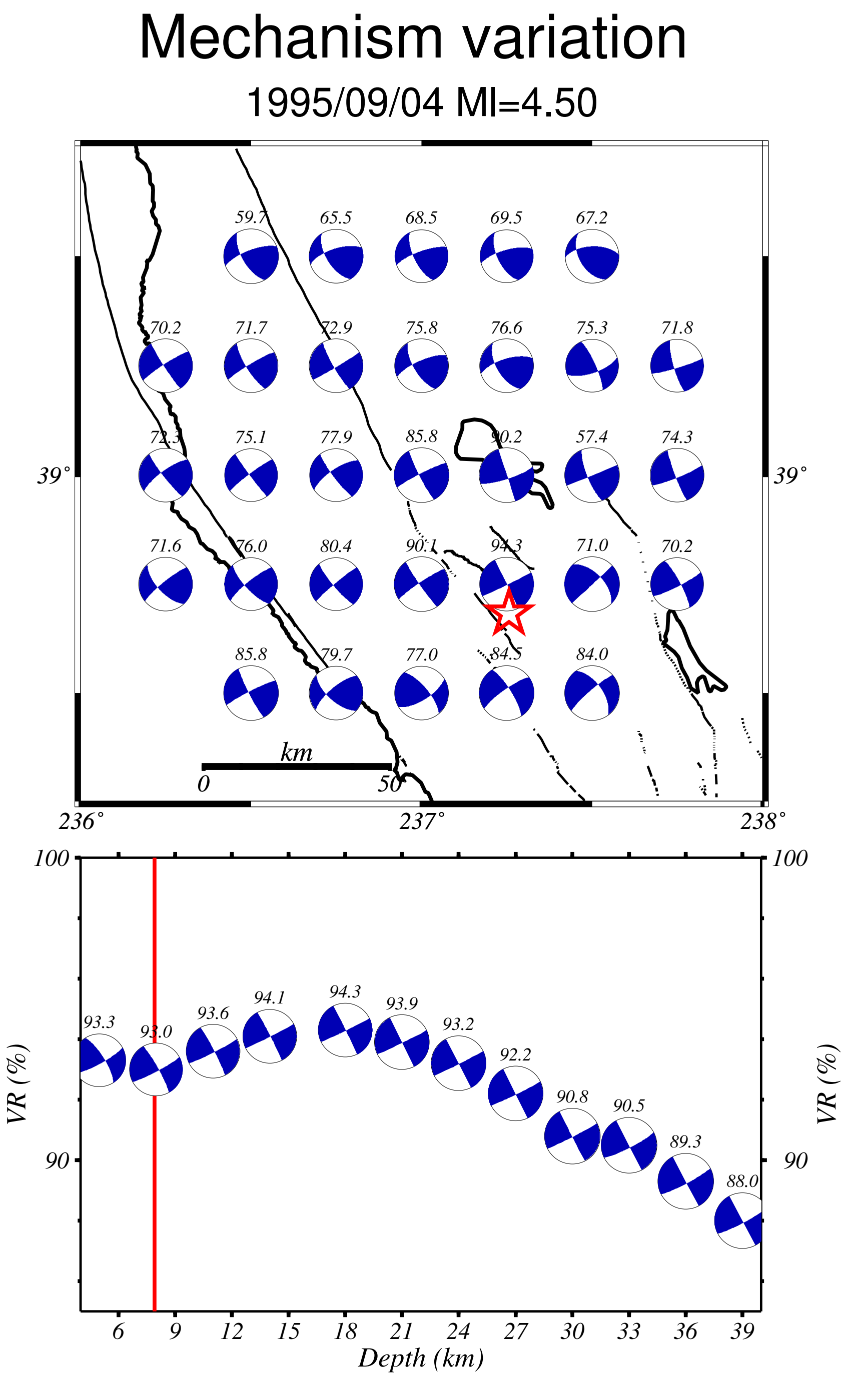

Figure 8 Same as Figure 6 for the Geyser event of figure 7.

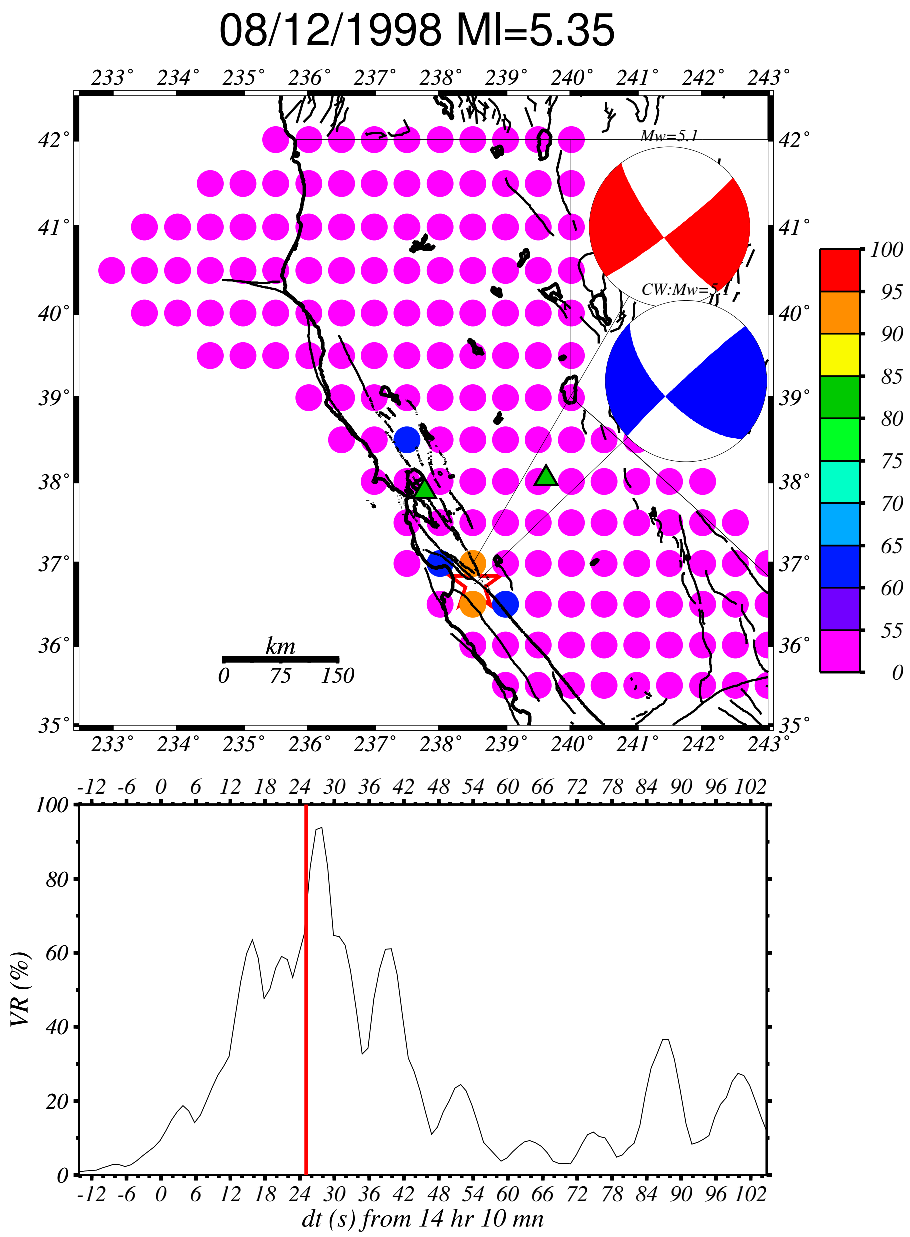

Figure 9 Same as Figures 5 & 7 for a 1998/08/12, $M\ell = 5.4$, San Juan Bautista event.

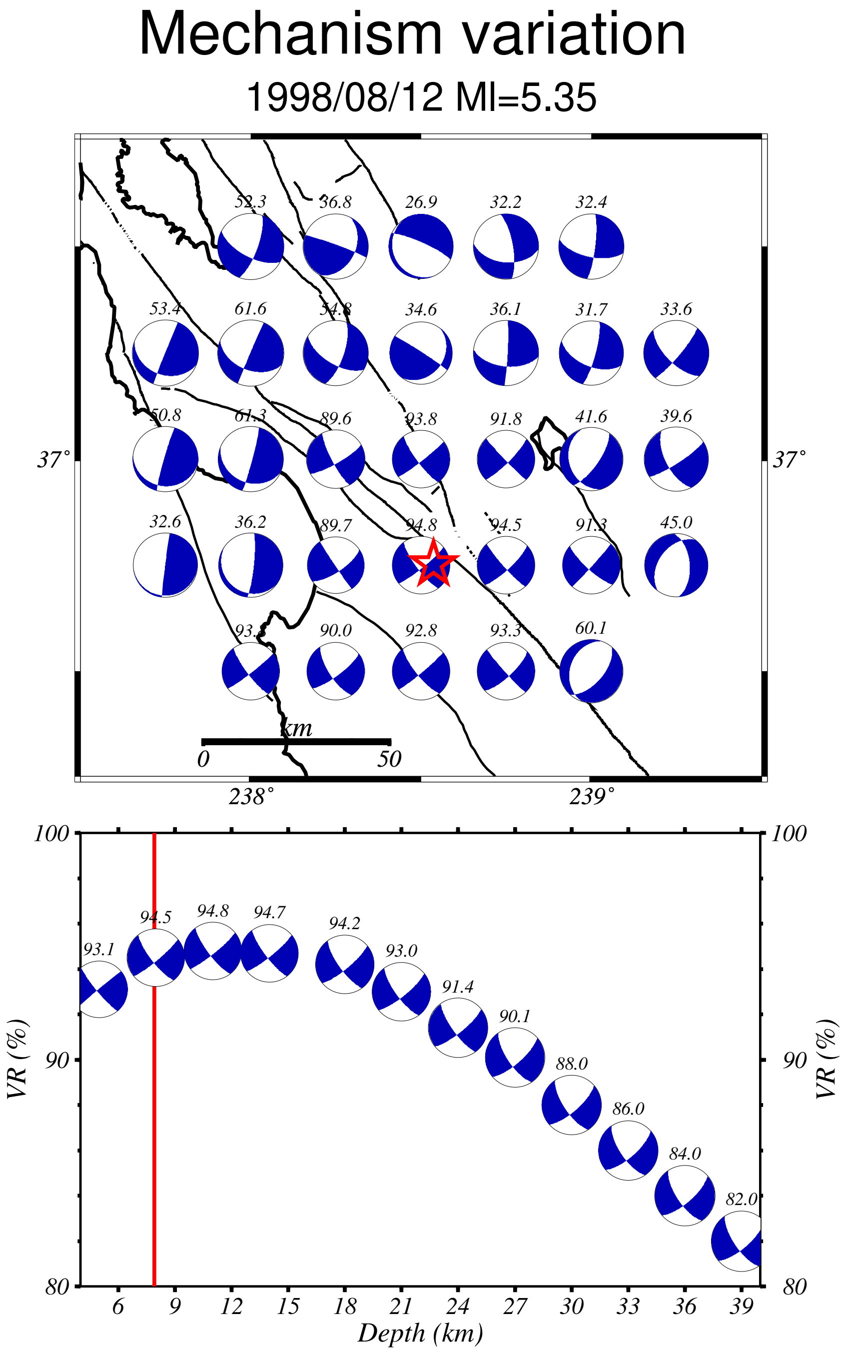

Figure 10 Same as Figures 6 & 8 for the San Juan Bautista event of figure 9.

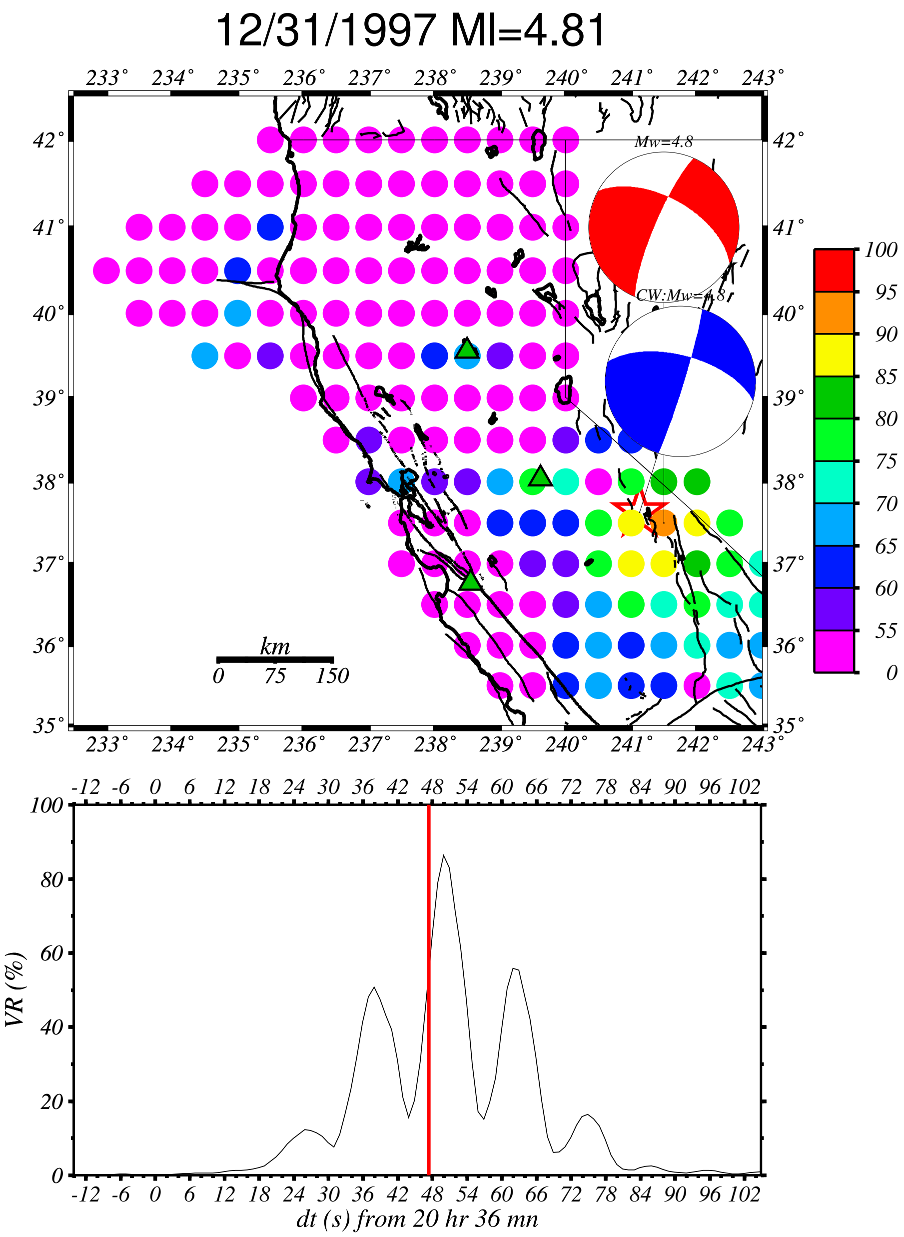

Figure 11 Same as Figures 5, 7 & 9 for a 1997/12/31, $M\ell = 4.8$, Mammoth event.

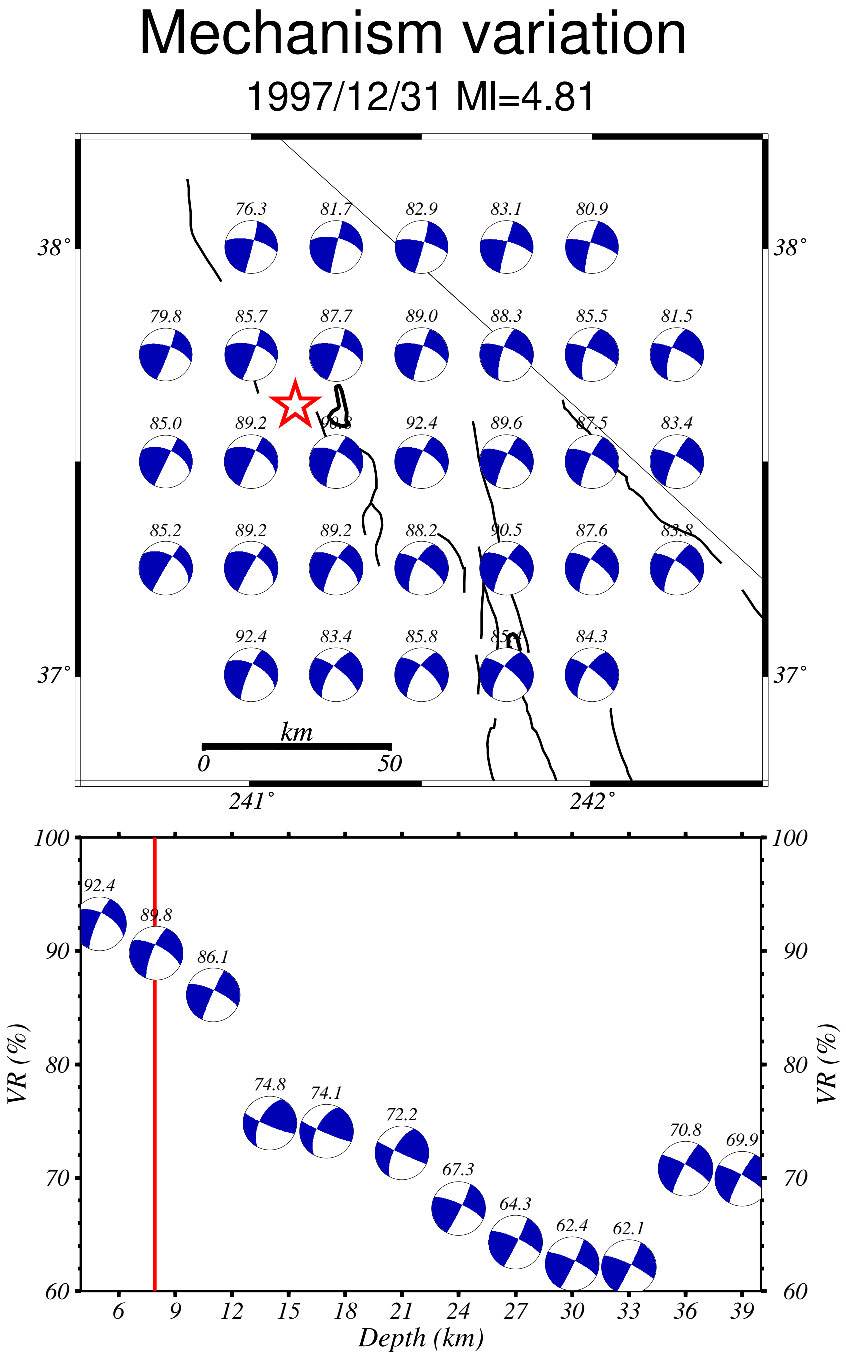

Figure 12 Same as Figures 6, 8 & 10 for the Mammoth event of figure 11.

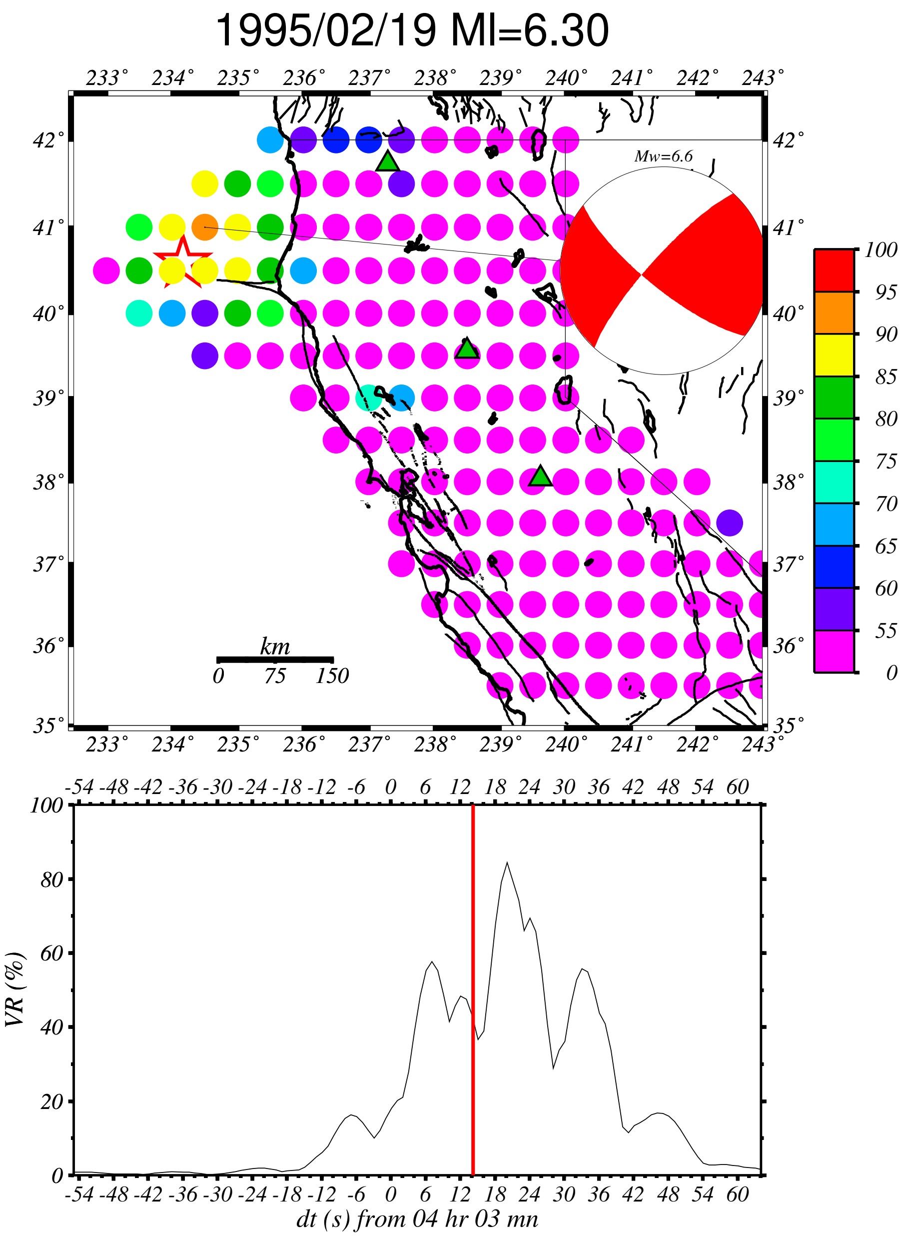

Figure 13 Same as Figures 5, 7 & 9 for a 1997/12/31, $M\ell = 6.8$, offshore Mendocino event.

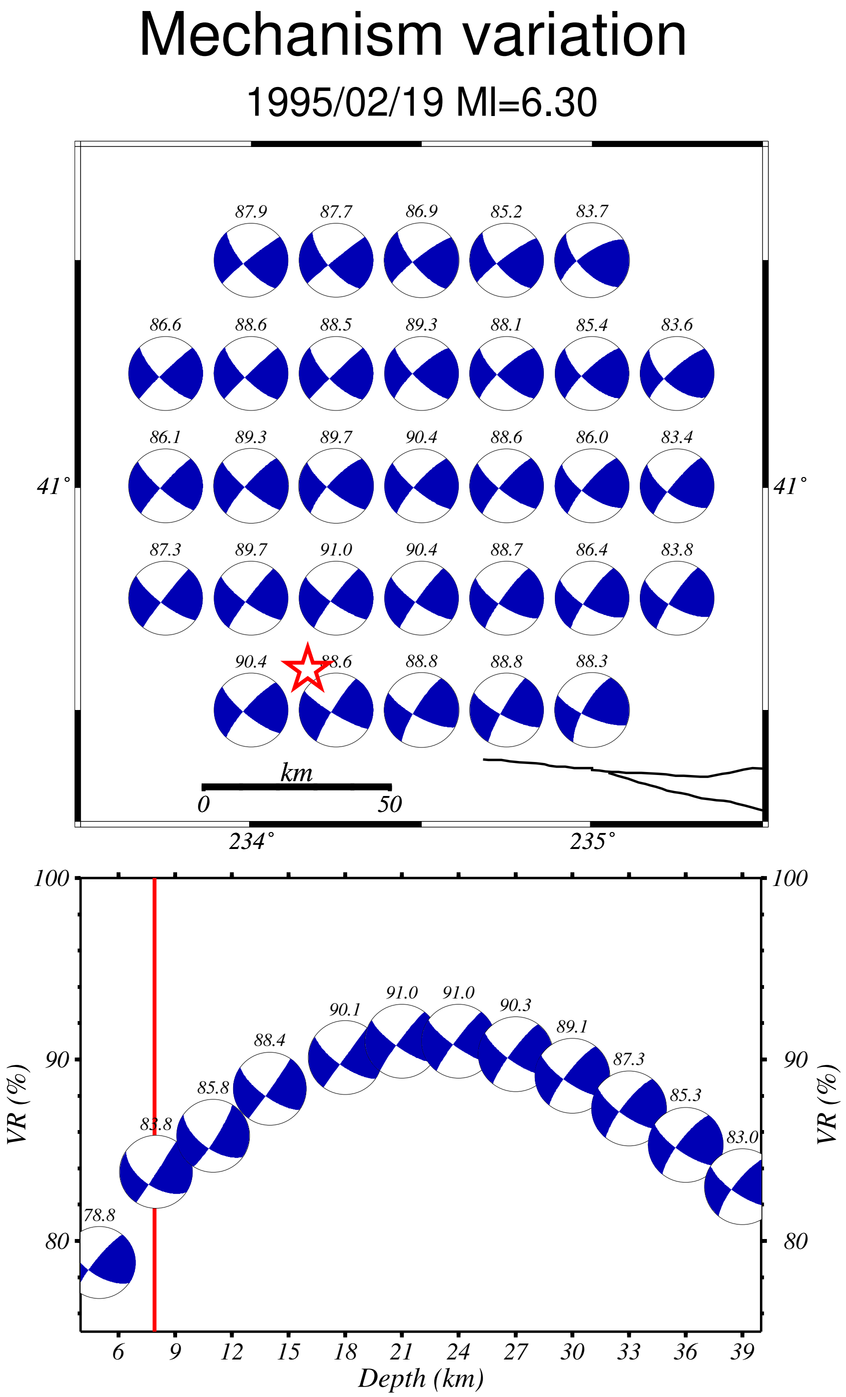

Figure 14 Same as Figures 6, 8 & 10 for the offshore Mendocino event of figure 11.

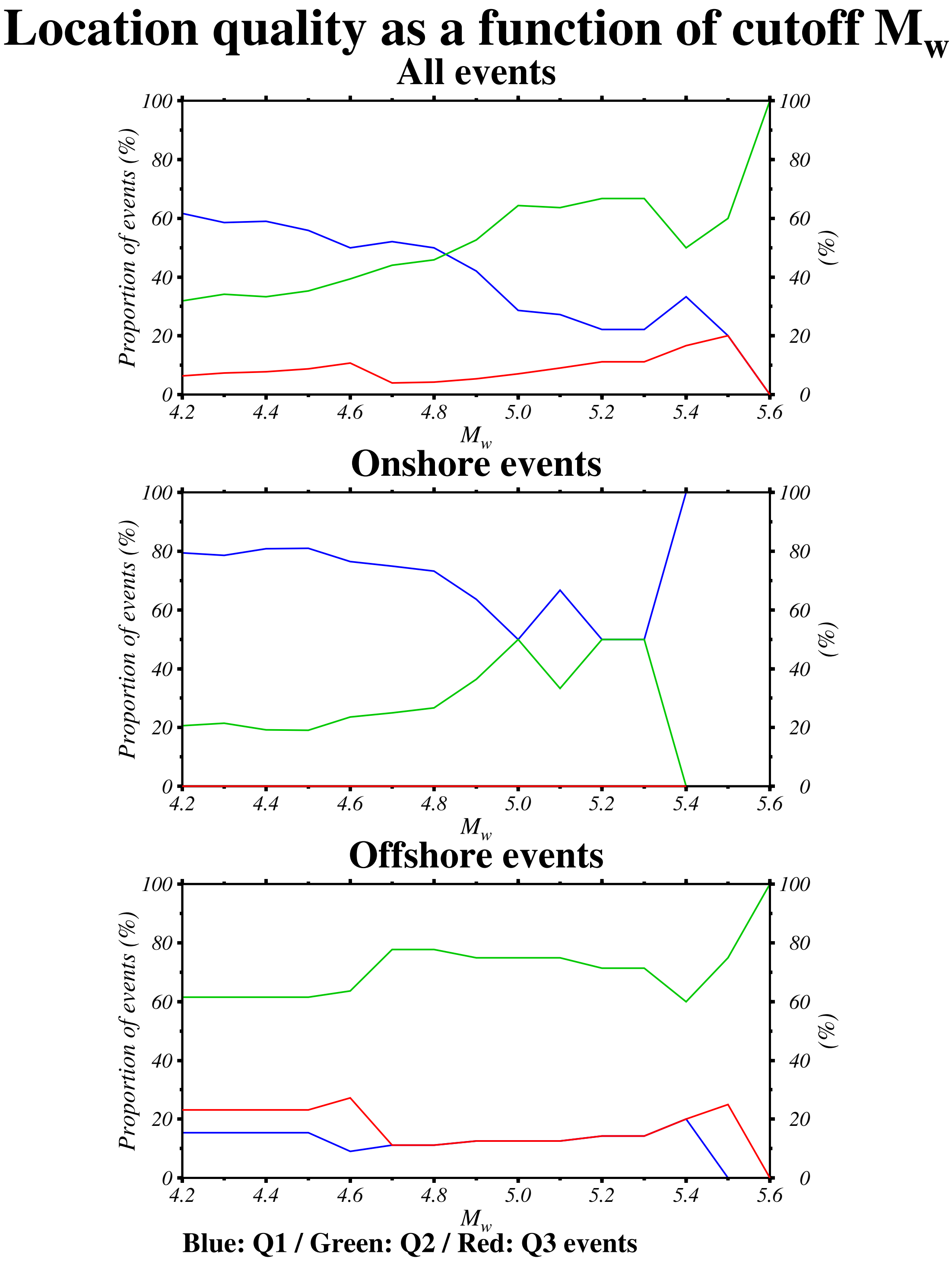

Figure 15 Trade-off curves showing the proportion of Q1 (blue line), Q2 events (green line) and Q3 events (red line) for a given M_w.

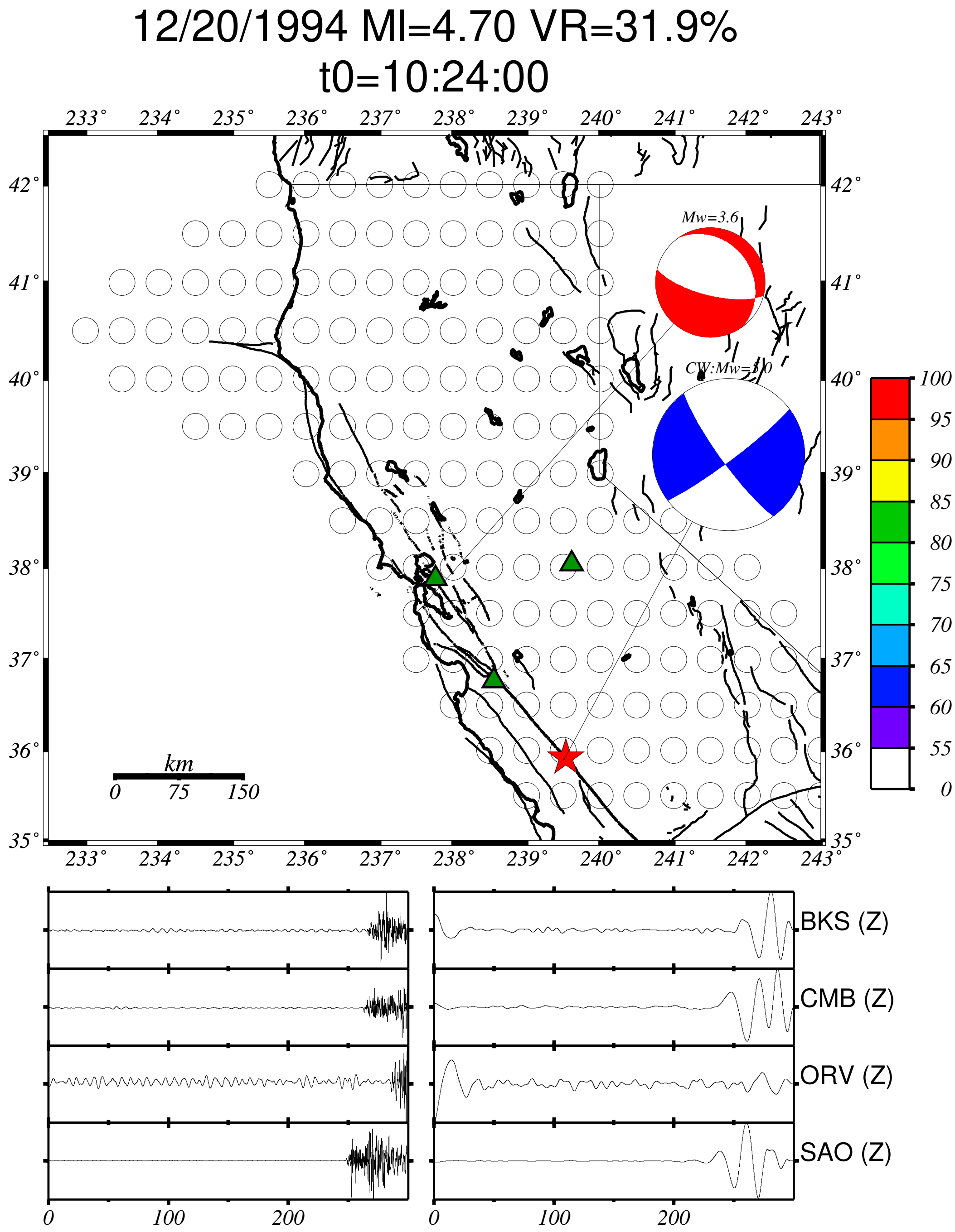

Figure 16 Frame 4 of the animation for the 12/20/1994 Parkfield event (M_ℓ=4.7, origin time 10:27:48). The waveforms barely enter the window which spans five minutes between 10:24:00 & 10:29:00. **VR** is low (31.9%). Poor agreement is found between the *AMT* and the *REDI* locations and MTs.

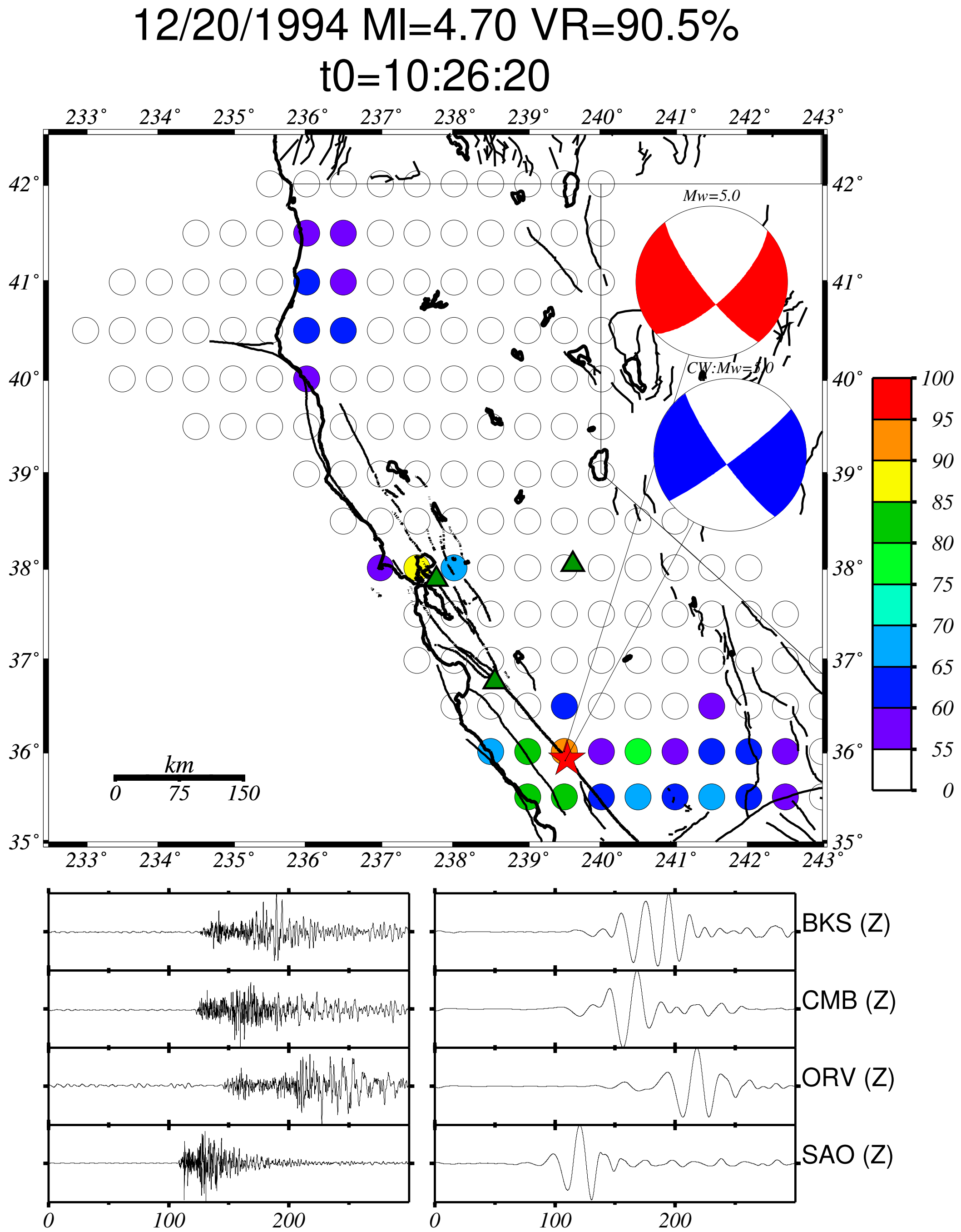

Figure 17 Frame 11 of the animation. The time windows include 5 mn of waveforms from 10:26:20. **VR** peaks at 90.5%. Good agreement is found between the *AMT* and the *REDI* locations and MTs.

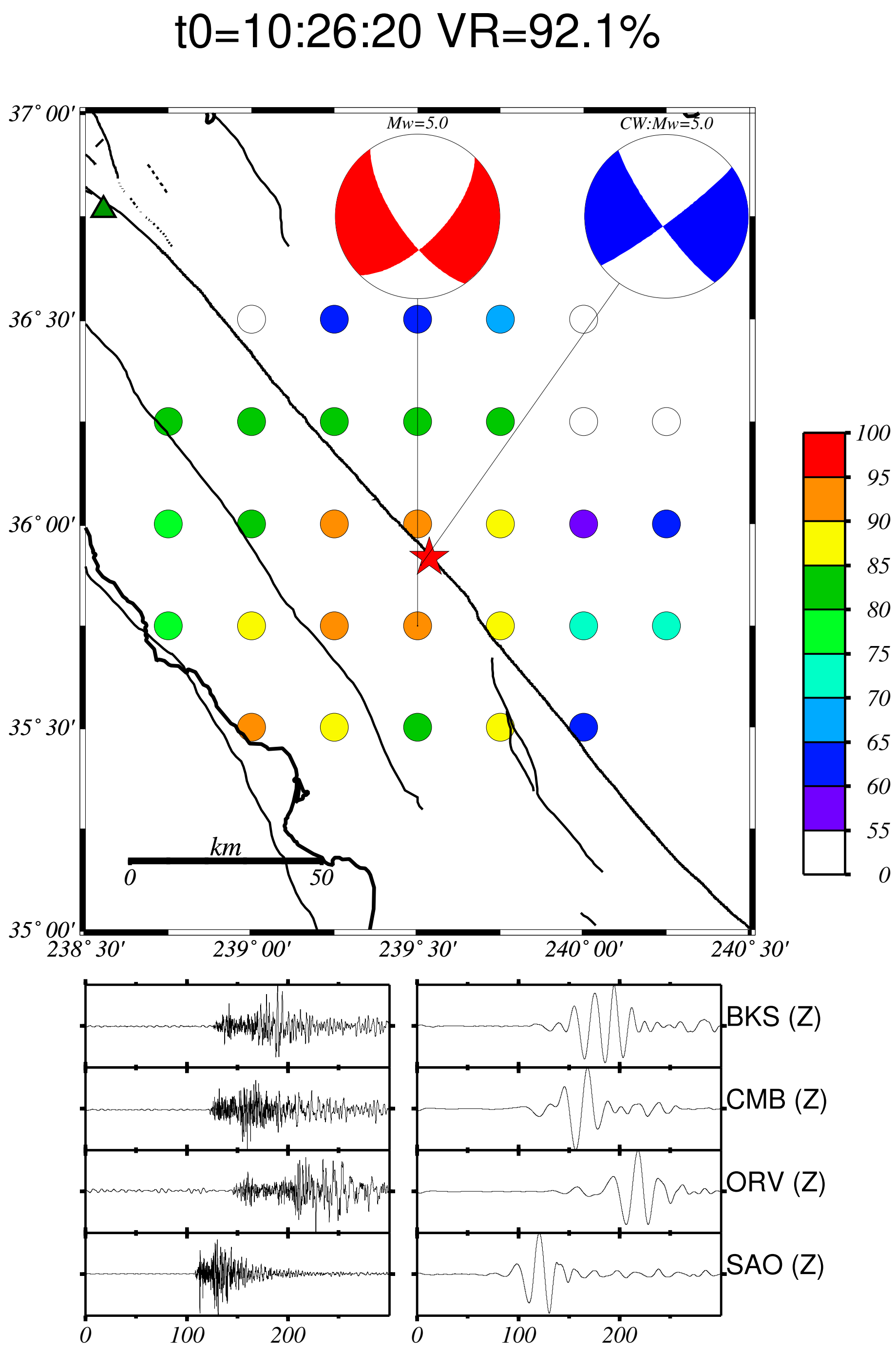

Figure 18 Frames 12-14 of the animation. The time windows include the same waveforms as Figure 17, but the inversion is conducted over the narrow $0.25° \times 0.25°$ grid about that solution. **VR** is 92.1%. Agreement between *AMT* and *REDI* solutions is improved, both in terms of location and MT (see Table 6).

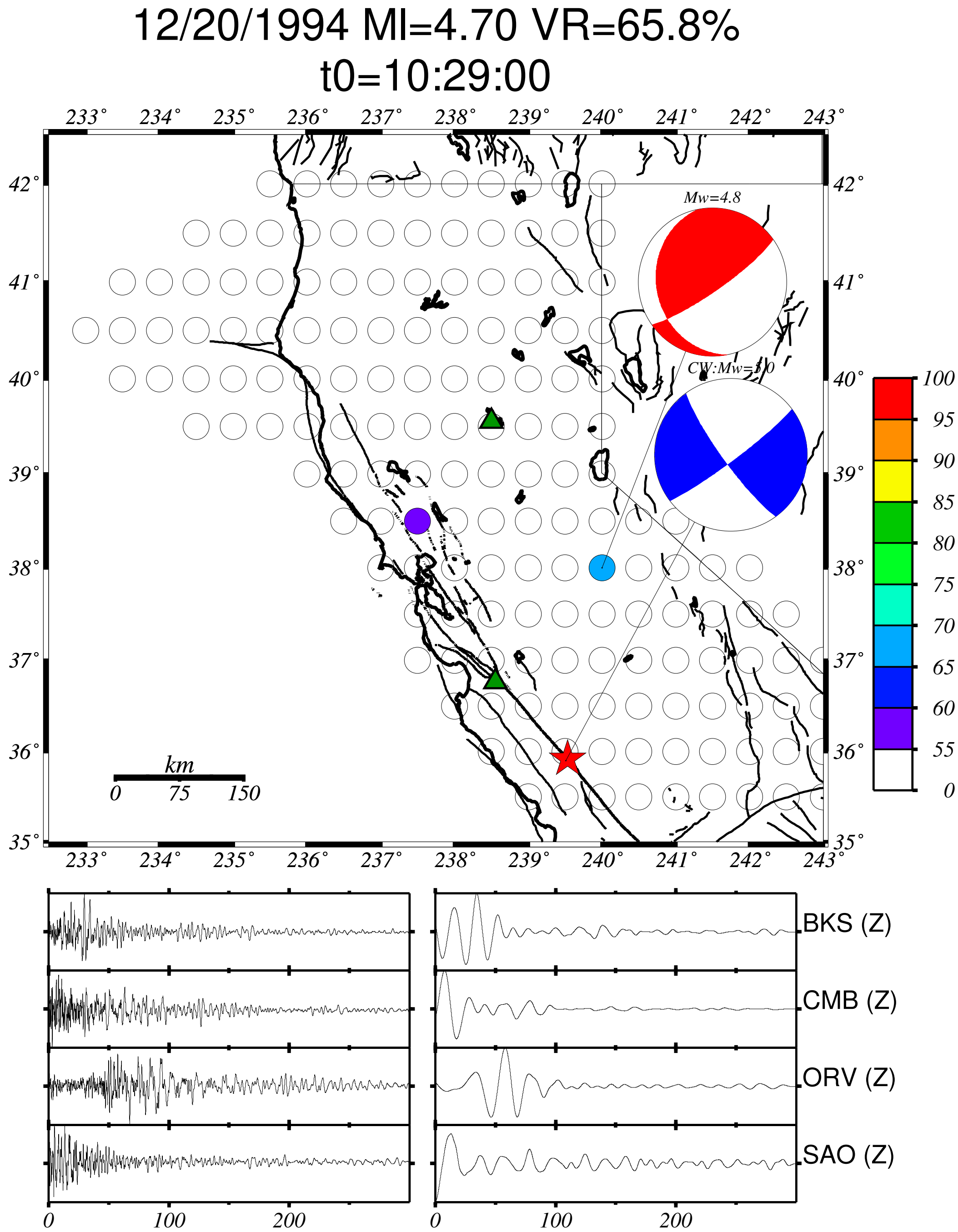

Figure 19 Frame 22 of the animation. The front part of the seismic wavetrain is outside of the widow. **VR** is 65.8%. Agreement between the *AMT* and the *REDI* solutions is lost.

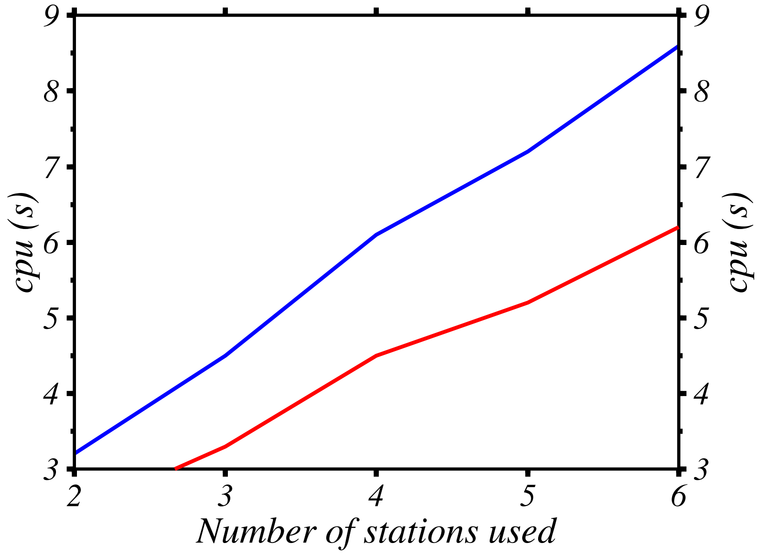

Figure 20 CPU time required to compute MT and depth, as a function of the number of stations used at a given source location. Blue: the Green's functions are read for each source location. Red: The GFs are stored in memory. This test was performed on a 250 MHz Ultra Sparc 2 workstation.